UNIVERSITY OF LEEDS

This is a repository copy of *A generalized multiphase modelling approach for multiscale flows*.

White Rose Research Online URL for this paper:
https://eprints.whiterose.ac.uk/172777/

Version: Accepted Version

Article:
De Santis, A orcid.org/0000-0002-9114-3394, Colombo, M orcid.org/0000-0002-4335-4250, Hanson, BC orcid.org/0000-0002-1720-1656 et al. (1 more author) (2021) A generalized multiphase modelling approach for multiscale flows. Journal of Computational Physics, 436. 110321. ISSN 0021-9991

https://doi.org/10.1016/j.jcp.2021.110321

© 2021, Elsevier. This manuscript version is made available under the CC-BY-NC-ND 4.0 license http://creativecommons.org/licenses/by-nc-nd/4.0/.

Reuse
This article is distributed under the terms of the Creative Commons Attribution-NonCommercial-NoDerivs (CC BY-NC-ND) licence. This licence only allows you to download this work and share it with others as long as you credit the authors, but you can't change the article in any way or use it commercially. More information and the full terms of the licence here: https://creativecommons.org/licenses/

Takedown
If you consider content in White Rose Research Online to be in breach of UK law, please notify us by emailing eprints@whiterose.ac.uk including the URL of the record and the reason for the withdrawal request.

White Rose university consortium
Universities of Leeds, Sheffield & York

eprints@whiterose.ac.uk
https://eprints.whiterose.ac.uk/

A generalized multiphase modelling approach for multiscale flows

A. De Santis[a,*], M. Colombo[a], B. C. Hanson[a], M. Fairweather[a]

[a] *School of Chemical and Process Engineering, University of Leeds, LS2 9JT, Leeds, United Kingdom*

Abstract

Multiphase flows are ubiquitous both in nature and industry. A broad range of interfacial scales, ranging from fine dispersions to large segregated interfaces, is often observed in such flows. Standard multiphase models rely on either the interface-averaging approach, which is suitable for the modelling of dispersed flows, or on the interface-resolving approach, which is ideal for large segregated interfaces. This results in the inability of such models to deal with complex multiscale flows, and different generalized hybrid modelling approaches having been proposed to overcome this shortcoming. This work presents a novel generalized multifluid modelling approach where large segregated interfaces are identified in the multifluid field from the local interface topology and resolution, avoiding the need for a-priori thresholds of the local volume fraction used in the majority of the models available in the literature. Interface compression and suitable modelling closures for drag and surface tension are activated in the large interfaces regions, whilst the model reverts to a standard multifluid formulation in the regions of small/dispersed interfaces. An assessment against different benchmark cases shows that the approach is as accurate as one-fluid interface-resolving techniques for large/segregated interfaces, while successfully recovering the expected multifluid behaviour for fully dispersed flows. Further, a prototypical multiscale flow has been simulated to demonstrate that the model can effectively switch between large-interface and dispersed-interface mode based on the local flow conditions and mesh size. It is concluded that the present approach represents a promising step towards the development of a comprehensive multiphase model capable of simulating complex multiscale flows of industrial interest.

Keywords: Multiphase flows, Interface resolution, Multiscale flows, Generalized model, Multifluid model

1. Introduction

Multiphase flows are found in several industrial applications ranging from liquid-liquid extraction processes in the nuclear industry to the multiphase flow in pipelines in the oil and gas industry. These flows are also widespread in nature, spanning from the flow in the human cardiovascular and respiratory systems to wave break-up and waterfalls. Compared to single-phase flows, multiphase flows pose additional challenges in terms of modelling; this is mainly due to the discontinuity represented by the interface between the phases and the need to account for interfacial transfer phenomena. Consequently, from the modelling point of view, it is convenient to classify multiphase flows based on their characteristic interfacial scale: this results in a broad distinction between small interfacial scale dispersed flows (e.g.: bubbly flow, droplet flow) and large interfacial scale segregated flows (e.g.: film flow, stratified flow in horizontal pipes) [1]. A schematic representation of these two flow typologies is given in Figure 1. The figure also depicts a numerical grid, to highlight the fact that in the numerical modelling context "large" and "small" interfaces are not absolute categories, but are relative to the local mesh size.

This classification corresponds to two distinct multiphase modelling approaches, i.e. interface-averaging and interface-resolving [2]. The interface-averaging approach assumes scale-separation

*Corresponding author. Tel.: +44 (0)113 343 2444 - E-mail address: a.desantis@leeds.ac.uk

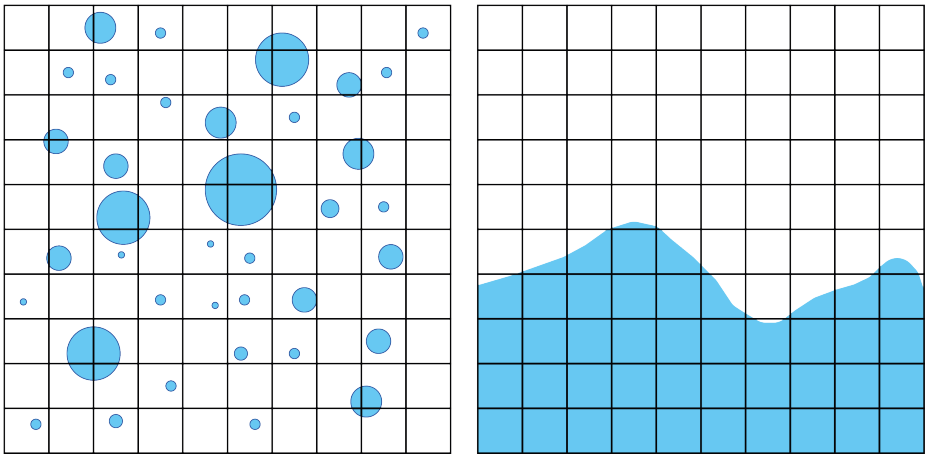

Figure 1: Schematic representation of small-scale interface (left) and large-scale/segregated interface (right) configurations, compared to the numerical grid resolution.

between the Dispersed Phase Elements (DPEs) and the macroscopic continuous phase. This allows for conditional volume-averaging of the governing equations, which leads to the so-called multifluid (or Eulerian) models. Within the multiphase system, all the phases share the same pressure and the different phases are treated as interpenetrating continua; each phase having its own momentum equation. This approach does not seek to resolve explicitly the morphology of the interface, which is lost in the averaging operation; consequently, the coupling between the phases is achieved by introducing suitable closures for the interfacial transfer terms appearing in each phase momentum equation. Similar closures are needed for the interfacial transfer of heat and mass. In the interface-resolving approach, in contrast, all the phases share the same momentum equation and the interfacial morphology is explicitly resolved. This requires the numerical grid to be fine enough to guarantee an adequate resolution of the interface, which usually limits the applicability of this approach to large-scale/segregated interfaces or dispersed flows with only a few DPEs. The interface-resolving approach leads to interface-tracking and interface-capturing models. In the former, the evolution of the interface is tracked in a Lagrangian fashion. In the latter, the interface is reconstructed from a known indicator function. Interface capturing approaches include the Level Set [3] and the Volume of Fluid (VoF) [4, 5] methods; Level Set and VoF represent the standard choices for the modelling of large-interface and free surface flows in industry. The numerical diffusion of the indicator function tends to introduce some degree of "smearing" of the interface in interface-tracking methods; therefore, special numerical treatments are required to counteract this effect [5]. In this context, the authors have recently developed a combined Level Set/VoF method applicable to unstructured meshes and demonstrated that this can lead to accurate predictions for prototypical large-scale/segregated multiphase flows [6].

However, the main limitation of the interface-resolving approach in the simulation of complex multiscale flows is the spatial grid resolution, and the related computational costs, necessary to resolve the entire range of interfacial scales. This has been highlighted, for instance, in the recent investigation of a Pulsed Sieve-plate Extraction Column performed with a coupled VoF/LES approach [7]. The work highlighted how an extremely fine mesh would be required to resolve the interfacial scales for the fine droplet dispersion expected in the region containing the sieve-plates, resulting in a prohibitive computational cost. On the other hand, in this as in many other engineering systems, it is crucial to account for the presence of such small-scale DPEs, since these are expected to contribute significantly to the mass transfer within the device due to their high interfacial area density. Therefore, there is a need for a computational tool that is equally applicable to all the flow regimes and scales encountered in the column, and which combines the features of both the interface-averaging and the interface-resolving approaches. More generally, multifluid and interface-capturing models

are the workhorses for multiphase flow modelling in industry, and they can provide accurate results when applied to flows that comply with the underlying modelling assumptions, i.e. scale-separation for the former and an adequate spatial resolution of the interface for the latter. However, as pointed out above, a broad range of interfacial scales coexists in most multiphase flows of practical interest, which can lead to local breakdown of the interface-averaging and interface-resolving modelling assumptions [8]. In the past few years, this has led to the development of a number of so-called generalized or "hybrid" models, aiming at handling the multiscale nature of multiphase flows. This is usually achieved by introducing some form of interface-capturing capabilities within the multifluid modelling framework. One of the first attempts in this direction is represented by the work of [9], in which the authors coupled the VoF and the multifluid approaches by using a switching function based on the value of a dispersion function defined using the average value of the gradient of the volume fraction evaluated on a 3×3 cells stencil for two-dimensional problems. A VoF formulation is employed in the cells where the dispersion function value is less than a critical threshold specified by the user, whilst a standard two-fluid formulation is used in the other cells; the specification of a suitable value for the user-defined dispersion threshold is a critical aspect of the model. In addition, a one-fluid approach is enforced in the VoF regions, which makes the transition between the one-fluid and the two-fluid approaches numerically cumbersome.

In their model, [10] coupled a two-fluid model with an interface-resolving approach for gas-liquid systems, and developed an unified solution framework to couple the two formulations in a numerically efficient way. In this approach the gas phase is split into two distinct fields, one representing the small-scale dispersed bubbles and the other one representing the large-scale gas regions, for which a VoF-like interface capturing approach is used; this results in a three-field/two-fluid model.

Successively, other authors such as Tomiyama et al. [11] and Alajbegovic and Han [12] have tried to couple the benefits of interface resolving and multifluid formulations, and a comprehensive review on the subject can be found in Marschall [2]. Overall, it has been recognized that including interface resolution-like features locally within the multifluid approach reduces the complexity of the model formulation by avoiding the cumbersome one-fluid/multifluid transition within the same computational domain [8, 13, 14]. Therefore, in the majority of the most recent works, the latter approach has been followed. Specific methods are implemented to detect the presence of a large interface and counteract the numerical diffusion this is naturally subjected to in a multifluid model, but each phase maintains its own momentum equation. In this way, the shape and the morphology of the interface are captured (similarly to the VoF approach), but the interfacial transfer processes still require modelling in order to couple the phase-specific momentum equations. However, the knowledge of the interface morphology allows for the local application of the most appropriate set of closures. This modelling concept is referred to as the large-interface or multifluid interface-resolving mode in the remainder of this paper.

Strubelj et al. [13] implemented interface sharpening within a two-fluid model to simulate free surface flows with large interfacial scales. An interface sharpening algorithm derived from the level set method of Olsson and Kreiss [15] is implemented and the large interface modelling includes drag and surface tension forces, the latter being evaluated using the local volume fraction as the weighting factor. The model is applied to cases where only segregated interfaces are present, and the criteria used for the choice between segregated and dispersed closures are not specified. Successively, the switch criterion originally introduced in the work of [9] has been added to the model formulation in [16]; this lead to a coupled two-fluid model which uses a standard dispersed two-fluid formulation in the regions where small interfacial length scales are recognized, whilst a two-fluid model including interface sharpening is used in the regions of large interfacial scales. The model has been successfully applied to simulate the contemporary presence of a large scale stratified interface and small "subgrid" DPEs within the same computational domain for a Rayleigh-Taylor instability test case. The model, however, inherits the shortcomings associated with the identification of a suitable value for the switch threshold highlighted above for the formulation of [9].

Marschall [2] and Marschall and Hinrichsen [17] rigorously derived the conservation equations of their hybrid interface-resolving two-fluid model (HIRES-TFM) using conditional spatial averaging.

The model is designed to handle, in a multifluid framework, averaged and resolved interfaces, as well as intermediate scales with a partially penetrating continua concept. Modelling closures for dispersed and segregated interfaces, the latter including drag, surface tension and interfacial pressure, are also rigorously derived. A dam break in the presence of an obstacle, described in detail in Section 4.2, was used as one of the test cases for model assessment. This is a popular test case for interface-resolving models, but it also features the presence of small dispersed droplets and entrained air bubbles. However, the HIRES-TFM formulation only included closure terms for the segregated flow type, and therefore the behaviour of the dispersed droplets and bubbles was not captured adequately; this is due to the lack of a mechanism to identify dispersed and segregated regions in the flow, and consequently select suitable closures for these regimes locally.

The Helmholtz-Zentrum Dresden-Rossendorf has developed a GENeralized TwO-Phase flow concept (GENTOP) [18] for gas-liquid systems, which represents an evolution of the Algebraic Interfacial Area Density [19] method. Similarly to the approach of [10], this model also employs a three-field/two-fluid concept, where the gas within the system is split into two distinct phases: a dispersed gas phase and a continuous gas phase, the latter representing large gas interfacial structures the numerical diffusion of which is prevented with the addition of a local clustering interfacial force. These large gas structures are identified via a free surface indicator field, which is defined as a function of the gradient of the volume fraction. The blending of interfacial momentum transfer models suitable for either dispersed or large interfaces and the activation of the clustering force are controlled by a blending method expressed as a function of the local void fraction value. The GENTOP approach can be coupled with the inhomogeneous MUltiple SIze Group (MUSIG) population balance [20], thus allowing for the simulation of polydispersed gas flows with changing morphology from dispersed to large/segregated interfaces.

A similar approach has been followed by [21], where a Large Interface Model (LIM) is added to a standard two-fluid model to ensure a sound numerical treatment of the large interface regions present within the domain. The large interface regions are identified within the LIM by means of the gradient of a "sharpened" volume fraction field, obtained using interpolation with harmonic and anti-harmonic values to evaluate the gradient of the "sharp" volume fraction in each cell. Once the locations of the large-interface structures are identified, the interfacial transfer terms are modelled using ad-hoc closures calculated over a three-cell stencil across the interface. The model is specifically designed to address stratified liquid and gas flows and includes a drag formulation that adds a tangential component derived from a wall-like treatment of the interface. The contribution of the surface tension force is not included in the formulation.

Wardle [22] and Wardle and Weller [23] developed a hybrid model, where the segregated interface modelling is activated in the presence of large interfaces. Activation can be based, alternatively, on the local gradient of the void fraction, the interfacial scale resolution or the resolution of the dispersed phase length scale; a compression term is included to keep the interface sharp, together with a drag force evaluated using the Schiller-Naumann model [24] and a surface tension force derived from the continuum surface force (CSF) method of Brackbill et al. [25].

An approach similar to the one of GENTOP has been used in the work of [14], where a Large Scale Interface (LSI) model has been built on top of a standard two-fluid model to provide multiscale simulation capabilities. A blending method expressed as a function of the local volume fraction value is used to switch between large-scale and dispersed closures within the governing equations. Also, the drag model from Strubelj and Tiselj [16] and the multifluid surface tension model of [13] are used to account for drag and surface tension effects for the segregated/large-interface part of the model. Further, the interface sharpening method of [21] has been added to the LSI formulation in [26].

The Nuclear Research and Consultancy Group (NRG) recently proposed a Hybrid Dispersed-Large Interface Solver (HD-LIS) [27]. This model follows an approach similar to that of [18]; however, HD-LIS is a two-field/two-phase model, and diffusion of large interfaces is prevented by local activation of an interface compression term in the continuity equation, similarly to the concept used by [23]. The large interface regions, where interface compression is active, are identified by using

a-priori flow regime maps based on the local void fraction value [19]. Likewise, large-scale and dispersed closures for the interfacial momentum transfer are blended using the same flow regime map concept, and closures for the segregated regime include the drag model from Marschall [2] and the surface tension force.

A summary of the main features of the models described above is provided in Table 1. For clarity, only models entirely based on the multifluid framework are included. The table highlights the presence of an interface sharpening mechanism, how large interfaces are recognized inside the multifluid field and the models employed for drag and surface tension in the segregated regime.

The work presented here introduces a novel GEeneralized Multifluid Modelling Approach (GEMMA) for the simulation of multiphase flows characterised by a broad range of interfacial scales. The model is theoretically applicable to systems of n phases, and each phase is represented by a single volume fraction field. The model is based on the multifluid concept, but its generalized formulation is applicable to small/dispersed interfaces as well as to localized interfaces; the latter are identified as regions where the local size of the computational grid allows for an adequate resolution of the interface morphology. The model is an evolution of the work of [22] and is equipped with an improved method to control the local applicability of the different modelling closures. In particular, the method is focused on ensuring that appropriate closure formulations are applied based on the local degree of resolution of the interfacial morphology and of the dispersed phase scales, and therefore it is strongly dependent on the local flow topology and mesh size; in this sense, it surpasses most of the available models of this kind which overwhelmingly rely on a-priori functions of the volume fraction to control the local model formulation. This allows for fine control of the minimum local interface resolution to be reached in order to activate the large-interface mode within the model; this avoids the use of a-priori thresholds of the local volume fraction employed by most of the available models. Furthermore, the local switch status is used to control the interfacial transfer terms in the governing equations by means of a novel blending method, which allows recovery a standard multifluid formulation in dispersed-interface mode and, at the same, permits a physically sound large-interface formulation, including the surface tension force, in the regions where the switch is active. Localized interfaces are detected in the dispersed multifluid field with a unified algorithm that evaluates the local resolution of the scales associated with both the interfacial morphology and the dispersed phase. When conditions on the resolution of both are met, a physically sound large-interface formulation is employed; this formulation includes interfacial friction (which was not accounted for in [22]) via the drag-like closure of [2], a multifluid formulation for the surface tension force, and a numerical compression term to counteract numerical diffusion typical of multifluid models. Conversely, in the dispersed regime, a standard multifluid formulation is recovered. The blending between dispersed and localized interfaces is achieved using native OpenFOAM functionalities, which ensures that additional interfacial physics, such as heat and mass transfer, can be seamlessly included in the GEMMA formulation at later development stages. A thorough assessment of the GEMMA concept in different fundamental test cases, representative of large/segregated and dispersed regimes, and of multiscale flow conditions where both coexist, is presented, with the aim of highlighting the strengths and weaknesses of the approach. A description of the modelling concept is provided in Section 2. Subsequently, the results obtained in the different test cases are introduced and critically analysed in Section 4. Finally, conclusions and future work are discussed in Section 5.

2. The GEMMA concept

The GEMMA method is built on top of a standard multifluid solver. In this work, the approach has been implemented in the open-source CFD code OpenFOAM 6.0 [29, 30], using its built-in *reactingMultiphaseEulerFoam* solver as a starting point. This is a multifluid solver for n compressible phases and can account for both heat and mass transfer. The solver also includes a broad variety of models for the interfacial transfer of momentum, heat and mass and can be coupled to an inhomogeneous population balance [20] to evaluate the local size distribution of the dispersed phase.

This work focuses on incompressible, adiabatic flows without mass transfer. Under these assumptions, the momentum conservation equation for phase k, derived from conditional volume averaging

Model	Interface sharpening method	Segregated interface detection	Segregated drag	Surface tension
Strubelj et al. [13, 16]	Not available in [13], conservative level-set method in [16] $\frac{\partial \alpha_k}{\partial t} + \nabla \cdot (\alpha_k (1-\alpha_k) n) = \varepsilon \Delta \alpha_k$	Not available in [13], method of [9] based on the volume fraction gradient in [16]	$\mathbf{F_d} = \alpha_1 \alpha_2 \rho_m \lvert \mathbf{U_r} \rvert \frac{C_d}{d} \mathbf{U_r}$	Volume fraction-weighted CSF $\mathbf{F_{st,k}} = \alpha_k \sigma \kappa \nabla \alpha_k$
HIRES-TFM [2, 17]	Not available	Not available	$\mathbf{F_d} = \lambda \lvert \nabla \alpha \rvert^2 \frac{\mu_1 \mu_2}{\mu_1 + \mu + 2} (\mathbf{U_2} - \mathbf{U_1})$	$\mathbf{F_{st,1}} = \alpha_1 4 \alpha_1 \alpha_2 \sigma [\nabla \cdot \left(\frac{\nabla \alpha_1}{\lvert \nabla \alpha_1 \rvert} \right) + 4 \Sigma_0 (1 - 2\alpha_1)] \nabla \alpha_1$
GENTOP [18]	Force between the liquid phase l and the continuous gas phase cg activated based on the local void fraction $\mathbf{F_{clust}} = -C_{clust} (1 - f_{fs}) f_{clust} \rho_1 \nabla \alpha_1$ $f_{clust} = [0.5 + 0.5 tanh [\alpha_B (\alpha_{cg} - \alpha_{clust,min})]] \cdot [0.5 + 0.5 tanh [\alpha_B (\alpha_{clust,max} - \alpha_{cg})]]$ $f_{fs} = 0.5 + 0.5 tanh [\alpha_{fs} \Delta (\lvert \nabla \alpha_{cg} \rvert - \lvert \nabla \alpha_{cg,crit} \rvert)]$	Interfacial area and drag formulations blended as a function of the local void fraction $f_{morph} = 0.5 + 0.5 tanh [\alpha_B (\alpha_{cg} - \alpha_{cg,crit})]$	$C_D = max(0.01, \frac{2 \left(\alpha_l \tau_{\mathbf{w,l}} + \alpha_{cg} \tau_{\mathbf{w,cg}} \right)}{\rho_l \mathbf{U_r}^2}$	Not included
Wardle [22]	Compression term in volume fraction equation $\frac{\partial \alpha_k}{\partial t} + \nabla \cdot (\alpha_k \mathbf{u}_k) + \nabla \cdot (\mathbf{u}_c \alpha_k (1 - \alpha_k)) = 0$	Can be set dependent on either: - Volume fraction gradient, or - DPE length scale, or - Local interface resolution	Schiller-Naumann [24], no segregated drag closure available	CSF [25]
LIM [21]	Volume fraction gradient evaluated using an interpolation based on harmonic and anti-harmonic values of the neighbouring cells	Local value of the volume fraction gradient larger than a critical value $\frac{\partial \alpha_k}{x_i} > \left(\frac{\partial \alpha_k}{x_i} \right)_{max} / r$	$\mathbf{F_d} = \alpha_k A_{D,n} \mathbf{U_{r,n}} + A_{D,t} \mathbf{U_{r,t}}$	Not included
LSI [14, 26]	Not available in [14], same method of LMI [21] in [26]	Drag and heat transfer blended using local void fraction $f = 1 - (1/f_a + 1/f_b)$ $f_a = 1 + exp [C (\alpha_g - \alpha_{min})]$ $f_b = 1 + exp [C (\alpha_{max} - \alpha_g)]$	$\mathbf{F_d} = \frac{1}{t_{ir}} \alpha_1 \alpha_2 \rho_m \mathbf{U_r}$	$\mathbf{F_{st,k}} = \alpha_k \sigma \kappa \nabla \alpha_k$
HD-LIS [27]	Compression term in volume fraction equation $\frac{\partial \alpha_k}{\partial t} + \nabla \cdot (\alpha_k \mathbf{u}_k) + \nabla \cdot (\mathbf{u}_c \alpha_k (1 - \alpha_k)) = 0$	Segregated and dispersed closures blended as a function of the local void fraction $f_c = \left[0.5 + 0.5 tanh \left[\frac{4}{c_1} (\alpha_{min} - \alpha_g) \right] \right] - \left[0.5 + 0.5 tanh \left[\frac{4}{c_1} (\alpha_g - \alpha_{max}) \right] \right]$	$\mathbf{F_d} = \lambda \lvert \nabla \alpha \rvert^2 \frac{\mu_1 \mu_2}{\mu_1 + \mu + 2} (\mathbf{U_2} - \mathbf{U_1})$	Density-corrected CSF [28] $\mathbf{F_{st}} = \frac{\rho_m}{\frac{1}{2}(\rho_1 + \rho_2)} \sigma \kappa \nabla \alpha$
GEMMA (present work)	Compression term in volume fraction equation $\frac{\partial \alpha_k}{\partial t} + \nabla \cdot (\alpha_k \mathbf{u}_k) + \nabla \cdot (\mathbf{u}_c \alpha_k (1 - \alpha_k)) = 0$	Binary C_α switch based on IRQ (Equation (5)) and (optionally) DPE length scale resolution (Equation (7))	$\mathbf{F_d} = \lambda \lvert \nabla \alpha \rvert^2 \frac{\mu_1 \mu_2}{\mu_1 + \mu + 2} (\mathbf{U_2} - \mathbf{U_1})$	Density-corrected volume fraction-weighted CSF (Equation (12))

Table 1: Summary of the main features of different hybrid multifluid models available in the literature.

of the local instantaneous momentum balance, reads

$$\frac{\partial \alpha_k \mathbf{u}_k}{\partial t} + \nabla \cdot (\alpha_k \mathbf{u}_k \mathbf{u}_k) = -\alpha_k \nabla p/\rho_k + \nabla \cdot (\nu_k \alpha_k \nabla \mathbf{u}_k) + \alpha_k \mathbf{g} + (\mathbf{F}_k + \mathbf{F}_{st,k})/\rho_k \tag{1}$$

where $\mathbf{F}_k$ includes the forces related to interfacial momentum exchange due to phase interaction, and $\mathbf{F}_{st,k}$ is the surface tension force.

The corresponding volume averaged continuity equation for phase k is

$$\frac{\partial \alpha_k}{\partial t} + \nabla \cdot (\alpha_k \mathbf{u}_k) = 0 \tag{2}$$

It should be noted that the advection equation for the indicator function used for interface-capturing in the VoF approach has the same form as Equation (2), except for the fact that the phase-specific velocity $\mathbf{u}_k$ is replaced by the one-fluid velocity $\mathbf{u}$ in VoF. One of the techniques used to counteract the numerical diffusion of the interface in the VoF context is to add a so-called compressive term to the advection equation of the indicator function [31]. Given the similarity of the latter with Equation (2), the same can be done in the multifluid approach to introduce some degree of interface sharpening [27, 23]. The continuity equation for phase k then becomes

$$\frac{\partial \alpha_k}{\partial t} + \nabla \cdot (\alpha_k \mathbf{u}_k) + \nabla \cdot (\mathbf{u}_c \alpha_k (1 - \alpha_k)) = 0 \tag{3}$$

where the term $\alpha_k (1 - \alpha_k)$ ensures that the compressive term is only active at the interface and $\mathbf{u}_c$ is the compressive velocity. The compressive term in Equation (3) does not correspond to any actual physical phenomenon, but is merely a numerical technique used to counteract another purely numerical effect, i.e. the smearing of the interface due to numerical diffusion. The compressive velocity is evaluated as

$$\mathbf{u}_c = C_\alpha |\mathbf{u}| \frac{\nabla \alpha}{|\nabla \alpha|} \tag{4}$$

where $\nabla \alpha_k / |\nabla \alpha_k|$ is the unit vector normal to the interface, and $|\mathbf{u}|$ is the magnitude of the relative velocity of the two phases at the interface. Upon discretisation of Equation (3), $|\mathbf{u}|$ is evaluated at the cell faces as a function of the face fluxes and of the gradient of the volume fraction [31]. The model coefficient C_α is a scalar which can theoretically take any positive value; in practice, in the VoF context, it is common practice to consider $C_\alpha = 1$ to limit parasitic currents, which are fostered at higher values. In *reactingMultiphaseEulerFoam*, the value of C_α can be specified for each phase pair within the system. $C_\alpha = 0$ corresponds to a standard multifluid formulation, whilst a value of 1 activates interface compression for a given phase pair; in the latter case the model will try to retain a sharp interface between the two phases of the pair in the entire domain.

In the GEMMA approach the C_α coefficient in Equation (4) becomes a binary field variable, following the principle outlined in [22]. A binary cell-centred C_α field is obtained from the switch logic described in Section 2.1. The face-centred $C_{\alpha,f}$ values are then obtained by means of central-differencing linear interpolation from the cell-centred values; this choice can potentially have a significant impact on the numerical results and will be investigated further as part of future model development and assessment. The binary C_α field is then used to switch dynamically between a standard interface-averaging multifluid formulation in the regions of small/dispersed interfacial scales and a multifluid interface-resolving formulation in the regions of large interfacial scales. The definition of "small" and "large" interfacial scales should be relative to the local mesh size and the capability of resolving those scales; therefore the switching criterion is strongly dependent on the numerical grid, and is described in detail in Section 2.1. In addition, the closures for the interfacial momentum exchange terms in Equation (1) have a different formulation in the dispersed and large interface regions, reflecting the different underlying physics; however, all the closures are expressed as a function of the same averaged variables available from the multifluid framework. Therefore, to ensure that consistent formulations are employed depending on the local interface description, both the surface tension force and the interfacial momentum transfer force in the momentum equation are expressed as a function of the local value of C_α, as detailed in Sections 2.2 and 2.3, respectively.

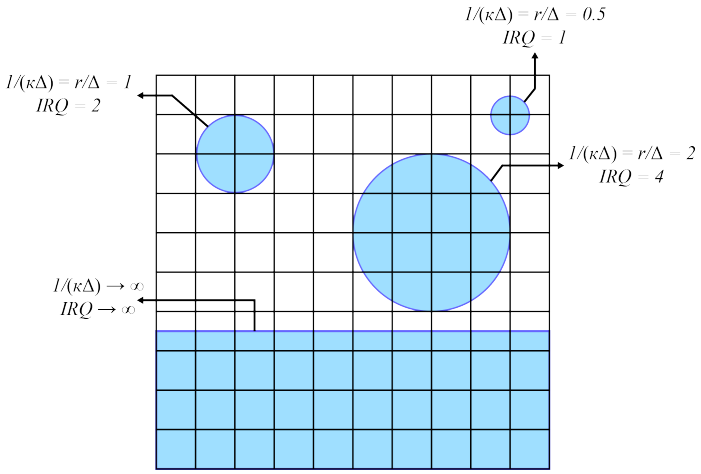

Figure 2: Two-dimensional representation of the IRQ criterion for circular DPEs of different size and for a segregated interface morphology.

2.1. Large-interface/dispersed-interface switch

The logic for the C_α switch devised within GEMMA is summarised in the flow-chart in Figure 3 and the key concepts behind it are described in this section. The main idea behind the switch logic is to link the activation of the large-interface mode to the local resolution of the interface morphology. Specifically, the large-interface mode should only be activated in regions where a desired resolution of the interface is achieved. This is quantified by introducing the Interface Resolution Quality (IRQ) index, originally proposed by [32], within the switching logic. IRQ is defined as

$$IRQ = \frac{2}{\Delta\kappa} \tag{5}$$

where Δ is the local mesh size and κ the local interface curvature. The former is taken equal to the cubic root of the mesh cell volume and the latter is evaluated geometrically from the volume fraction field as [33]

$$\kappa = -\nabla \cdot \left(\frac{\nabla\alpha}{|\nabla\alpha|} \right) \tag{6}$$

A schematic representation of the meaning of IRQ is provided in Figure 2. The figure makes use of the observation that, for a spherical DPE, it results in $\kappa = 1/r$; it can be seen that large values of IRQ correspond to a more accurate resolution of the interface. Therefore, the switching criterion in GEMMA relies on the introduction of a minimum threshold IRQ_{crit}; the local IRQ value has to be higher than the critical value specified by the user for the large-interface mode to be activated, as shown in Figure 3. In the successive step, minimum and maximum thresholds for the value of the dispersed phase volume fraction are introduced within the switch logic; threshold values of 0.01 for α_{min} and 0.99 for α_{max} are used in all the simulations performed in this work to ensure that interface-resolution is only activated in the proximity of the interface.

In the last logical step, if the local diameter of the dispersed phase d is known via a population balance, an additional check is performed to ensure that interface resolution is only switched on in the cells where the condition

$$d > \Gamma\Delta \tag{7}$$

is satisfied, i.e. where the dispersed phase diameter is larger than the local mesh size by at least a factor Γ; the latter is a user-specified parameter which allows further control by guaranteeing that each DPEs is resolved by at least Γ mesh elements for the multifluid interface-resolving mode to be activated.

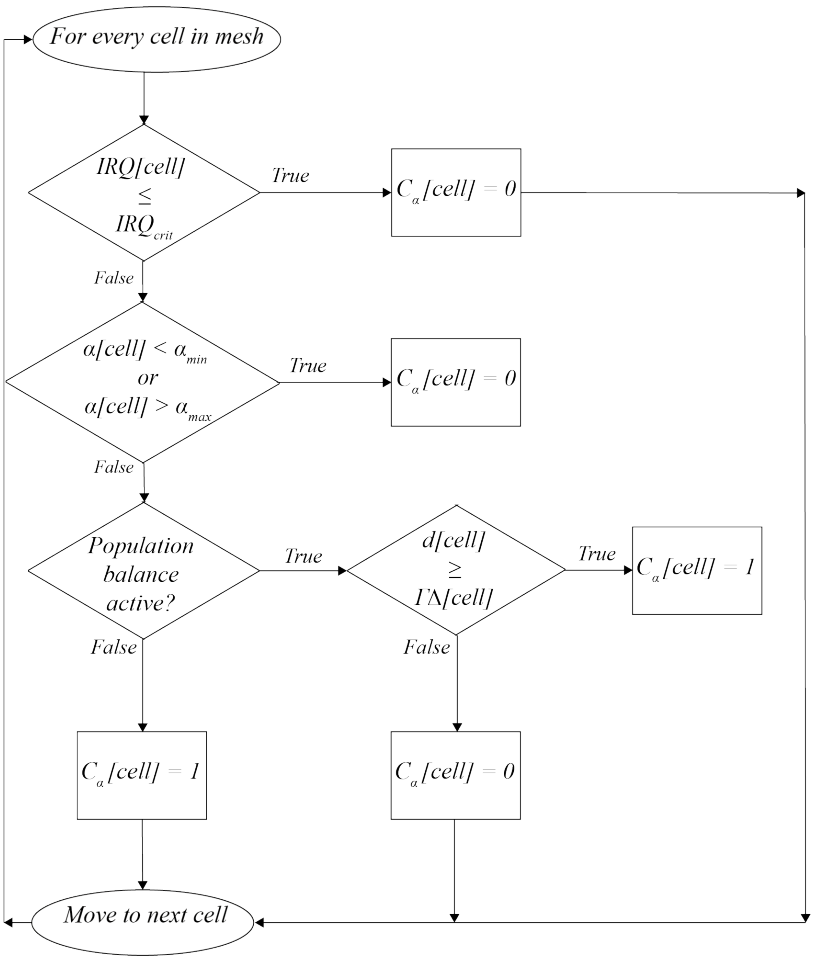

Figure 3: Flow-chart for the switching logic within GEMMA.

In a multifluid model, the modelling of the interfacial transfers of mass, momentum and energy is unavoidably related to the knowledge of the interfacial area across which these transfers take place. In dispersed regions where $C_\alpha = 0$, the interfacial area density is evaluated as

$$a_{i,DI} = \frac{6\alpha}{d_{32}} \tag{8}$$

where d_{32} is the Sauter mean diameter resulting from the population balance and the subscript DI stands for dispersed interface, which indicates that Equation (8) is only valid in the cells where $C_\alpha = 0$. Instead, in the cells where $C_\alpha = 1$ and the interface morphology is resolved, the interfacial area density is evaluated from the magnitude of the gradient of the volume fraction [34]

$$a_{i,LI} = |\nabla\alpha| \tag{9}$$

where the subscript LI stands for large interface. In the present version of the model, although the population balance and the switching logic are coupled via Equation (7), a change in the switch status does not have any effect on the population balance equation, which can lead to some local inaccuracies in the total balance of the interfacial area density. A complete coupling between the two approaches, by including source/sink terms in the population balance equation driven by changes in the local switch status, will be the focus of the next development phase. It is important to point out, however, that the correct interfacial area density formulation is used when modelling interfacial momentum transfer in large interface regions, with appropriate closures for the drag and the surface tension forces.

2.2. Surface tension implementation

The CSF method [25] is usually employed in the interface-resolving framework to account for surface tension effects in the momentum equation. This expresses the surface tension force as

$$\mathbf{F}_{st} = \sigma\kappa\nabla\alpha \tag{10}$$

where σ is the surface tension coefficient between a given phase pair. For systems where a large density difference is present between the different phases, it is advisable to include a density correction in Equation 10, to ensure that the surface tension force is only dependent on the density gradient and not on the density value itself [28]. The density-corrected CSF model results in

$$\mathbf{F}_{st} = \sigma\kappa\nabla\alpha\frac{2\rho}{\Delta\rho} \tag{11}$$

where ρ is the local mixture density and $\Delta\rho$ is the density difference between the two phases.

In addition, it should be noted that the calculation of the curvature using Equation (6) can be problematic, given the sharpness of the volume fraction field and the consequent numerical problems that can arise in the evaluation of its gradient; in particular, it has been observed that the calculation of the curvature based on a "sharp" volume fraction field in the CSF framework can facilitate the appearance of parasitic currents [28, 35]. For this reason, it is advisable to smooth the volume fraction field ahead of the calculation of κ. Within GEMMA, this is achieved using the Smoothed Continuum Surface Force (SCSF) method of [5], where the volume fraction field is smoothed by successive interpolation cycles from cell centres to cell faces.

Finally, one should note that CSF-based methods have been derived to be used in the one-fluid framework, where all the phases share the same momentum equation. In the multifluid approach, the total surface tension force given by Equation (11) should be somehow distributed among the phases occupying a given mesh cell. [13] showed that an effective way to achieve this is to use the local phase volume fraction α_k as a weighting factor. Furthermore, in the context of "hybrid" models, one should be careful to only include surface tension effects in large interface regions; within GEMMA, this is achieved by multiplying the surface tension force resulting from the modelling assumptions

outlined above by the switching function C_α, resulting in the following formulation for the surface tension force for phase k

$$\mathbf{F}_{st,k} = \alpha_k \sum_{i=1}^{n_k} \left(C_{\alpha_{k,i}} \sigma_{k,i} \kappa \nabla \alpha \frac{2\rho}{\Delta\rho_{k,i}} \right) \tag{12}$$

where the summation includes all the n_k phases which share an interface with phase k in a given mesh cell and the curvature κ is calculated on a smoothed volume fraction field following the SCSF approach.

2.3. Blending of the interfacial transfer terms

In Equation 1, the $\mathbf{F}_k$ term accounts for the interfacial forces (different from the surface tension force which is modelled via Equation (12)) that contribute to the interfacial momentum transfer between the phases. In the dispersed regime, this includes drag, lift, wall lubrication, virtual mass and turbulent dispersion forces

$$\mathbf{F}_{DI} = \mathbf{F}_d + \mathbf{F}_l + \mathbf{F}_w + \mathbf{F}_{vm} + \mathbf{F}_{td} \tag{13}$$

In regions of large interfaces, when the compressive term is active, interfacial friction can be evaluated from the local velocity field, obtaining a drag-like closure suitable for large interfacial scales. The blending between the dispersed and large-interface modes is achieved in a generalized way by building on the standard blending methods available in OpenFOAM [30]. These blending methods are used to take into account the variability of flow regimes in a multiphase flow and blend between formulations suitable for dispersed and large interfacial scales, covering phase-inversion situations. For a generic force $\mathbf{F}$ between two phases i and j the blending is given by

$$\mathbf{F} = (1 - f_i - f_j)\mathbf{F}_{LI} + f_i \mathbf{F}_{disp,ij} + f_j \mathbf{F}_{disp,ji} \tag{14}$$

In the previous equation, f is a blending function and the subscripts *disp,ij* and *disp,ji* refer to the phase i being dispersed in the continuous phase j and vice versa. In OpenFOAM, linear and hyperbolic blending methods are already available. In the linear method, the blending function is given by

$$f_i = max(0, min(1, \frac{(\alpha_j - \alpha_{j,min})}{(\alpha_{j,max} - \alpha_{j,min})})) \tag{15}$$

In the GEMMA approach, the blending is realised by including the local value of the switching function C_α in the blending expression, effectively obtaining a dependence on the local, time-dependent behaviour of the interface morphology. For the drag force the blending reads

$$\mathbf{F}_d = (1 - (1 - C_\alpha) f_i - (1 - C_\alpha) f_j)\mathbf{F}_{d,LI} + (1 - C_\alpha) f_i \mathbf{F}_{d,ij} + (1 - C_{alpha}) f_j \mathbf{F}_{d,ji} \tag{16}$$

Using Equation 16, only the large-interface drag formulation is active in large interface regions, but the model maintains the capability to cover the entire range of regimes from dispersed to a previously dispersed phase becoming continuous. Instead, for the forces that are neglected in the presence of large interfacial scales (i.e. lift, wall lubrication, virtual mass and turbulent dispersion), the blending becomes

$$\mathbf{F} = (1 - C_\alpha) f_i \mathbf{F}_{disp,ij} + (1 - C_\alpha) f_j \mathbf{F}_{disp,ji} \tag{17}$$

Equation 17 ensures that no force contribution is added when the compressive term is active.

Also, it is worth pointing out that the generalized blending method devised within GEMMA can be extended to closures for mass and heat interfacial transfer terms.

Equation	Term	Scheme
Momentum (Equation (1))	$\nabla \cdot (\alpha_k \mathbf{u}_k \mathbf{u}_k)$	Limited Linear
Continuity (Equation (3))	$\nabla \cdot (\alpha_k \mathbf{u}_k)$	van Leer
All	$\partial \bullet / \partial t$	1^{st} order Eulerian implicit

Table 2: Discretisation schemes for the convective and the time-derivative terms.

	$\mathbf{U_k}$	p_{op}	α_k
Inlets	fixedValue	fixedFluxPressure	fixedValue
Outlets	pressureInletOutletVelocity	totalPressure	zeroGradient
Walls	noSlip	fixedFluxPressure	zeroGradient

Table 3: Boundary conditions used for the phase velocity $\mathbf{U_k}$, the operating pressure p_{op} and the volume fraction α_k for different boundary types.

3. Numerical settings

All the simulations have been performed using the open-source CFD code OpenFOAM 6.0. The convective terms in all the transport equations have been discretised using second-order Total Variation Diminishing (TVD) schemes [27, 30]; the numerical schemes used for the convective and the time-derivative terms in all the simulations, unless otherwise specified, are summarised in Table 2.

The boundedness of the volume fraction equation is guaranteed by the semi-implicit MULtidimensional limiter for Explicit Solution (MULES) [31, 27] All the simulations have been performed using a multiphase extension of the transient PIMPLE pressure-velocity coupling algorithm [30]. This algorithm consists of a main SIMPLE-like [36] outer loop; another PISO-like [37] inner loop corrects the pressure for each iteration of the outer loop. If the number of outer loop cycles per time-step is set to one, PIMPLE reduces to the standard PISO algorithm.

The boundary conditions used for the different variables for different boundary types are summarised in Table 3. Unless otherwise stated, these boundary conditions have been employed in all the simulations. In OpenFOAM it is common practice to solve for the operating pressure $p_{op} = p - \rho g h$, which is equal to the static pressure p minus the hydrostatic contribution $\rho g h$ calculated with respect to a reference location [30]; therefore, the boundary conditions for the pressure outlined in Table 3 are specified with respect to p_{op}. The naming conventions used in OpenFOAM are referred to in Table 3. A short description of these conditions is provided here, and more details can be found in [30]. The *zeroGradient* condition corresponds to a standard Neumann condition, whilst *fixedValue* enforces a standard Dirichlet condition; *noSlip* is a wrapper around the latter used to enforce the no-slip condition at the walls for the velocity field. The *fixedFluxPressure* condition is used instead of *zeroGradient* for p_{op} for flows in which body forces such as gravity and/or surface tension are present; this condition adjusts the pressure gradient on the boundary so that the flux is equal to that specified by the velocity boundary condition on the same boundary. The *totalPressure* condition is used to enforce the operating pressure on the boundary as a function of a specified total pressure value p_0 as $p_{op} = p_0 - \frac{1}{2}\rho|\mathbf{u}|^2$; finally, *pressureInletOutletVelocity* is a Robin-type condition specific for the velocity field which enforces a Neumann condition on the boundary faces where the flow is leaving the domain and a Dirichlet condition based on the flux in the boundary-normal direction when the flow enters the domain.

The drag force (Equation (16)) and the surface tension force (Equation (12)) have been included in all the test cases; for the pipe flow case all the terms in Equation (13) are accounted for, since this case has been specifically included to test the behaviour of the whole dispersed modelling framework. For the large-interface drag force $\mathbf{F}_{d,LI}$, the model proposed in [2] is employed in all the test cases;

Test case	Expected interfacial morphology/scale	References
Ethanol droplet in equilibrium in air	Segregated/Large-scale	[27, 13]
Dam break in the presence of an obstacle	Segregated/Large-scale	[38, 39]
Rising bubble	Segregated/Large-scale	[6, 27, 40]
Dispersed flow in a vertical pipe	Dispersed/Small-scale	[41, 42, 43]
Water jet plunging in a quiescent pool	Hybrid/Multiscale	[18, 44, 45]

Table 4: Test cases summary.

	Density ρ (kg/m^3)	Viscosity μ $(Pa \cdot s)$
Air	1.1768	0.002
Ethanol	787.88	0.024
σ (N/m)	0.02361	

Table 5: Fluid properties for air and ethanol.

the large-interface drag force is expressed as

$$\mathbf{F}_{d,LI} = [0.5\frac{\rho_m \delta |\mathbf{U}_i - \mathbf{U}_j|}{\frac{\alpha_i \alpha_j \mu_i \mu_j}{\mu_i + m u_j}} + 8\frac{\frac{\alpha_i \alpha_j \mu_i \mu_j}{(\alpha_j \mu_j + \alpha_j \mu_i)}}{\frac{\mu_i \mu_j}{(\mu_i + \mu_j)}}]\frac{|\nabla \alpha|}{\delta}\frac{\mu_i \mu_j}{(\mu_i + \mu_j)}(\mathbf{U}_i - \mathbf{U}_j) \tag{18}$$

The specific models used for the dispersed-interface regions will be specified on a case-by-case basis in Section 4.

4. Results and discussion

This section reports the results obtained with the GEMMA approach in different test cases; the main aim here is to assess the performance of GEMMA in the simulation of multiphase flows characterised by different interfacial scales. Therefore, test cases representative of large/segregated interfaces, dispersed interfaces as well as a prototypical multiscale flow have been considered, as summarised in Table 4; these test cases have been widely used in the literature to assess multiphase modelling approaches with different interfacial morphologies.

4.1. Ethanol droplet in equilibrium in air

The generalized multifluid surface tension implementation used within GEMMA has been assessed in a simple test case proposed by [13]; the case consists of an ethanol droplet in equilibrium in air in the absence of gravity. The computational domain is a two-dimensional square of side L equal to 0.75 mm, with the four sides treated as no-slip walls. The ethanol droplet has a radius of 2 mm and is located at the centre of the domain. The mesh consists of a uniform 128×128 quadrilateral grid. The fluid properties for air and ethanol are reported in Table 5; as suggested in [27, 13], the viscosity values reported in Table 5 and used in the numerical simulations are increased by a factor of 20 with respect to the actual physical values to reduce the presence of parasitic currents in the velocity field and achieve a faster stabilization of the droplet shape. For this particular case, no dispersed-interface drag model is included in the model. Both fluids are treated as laminar and the simulation has been run for a flow time of 2 s. A switch based on the local IRQ value has been used, as described in Section 2.1, with $IRQ_{crit} = 2$.

The C_α and the ethanol volume fraction contours obtained with the GEMMA approach are shown in Figure 4. It can be seen how the switching criterion can identify the presence of the interface between the ethanol droplet and the surrounding air correctly; consequently, large-interface mode is activated in the interfacial region, as can be seen from the sharp interface visible in the zoomed-in

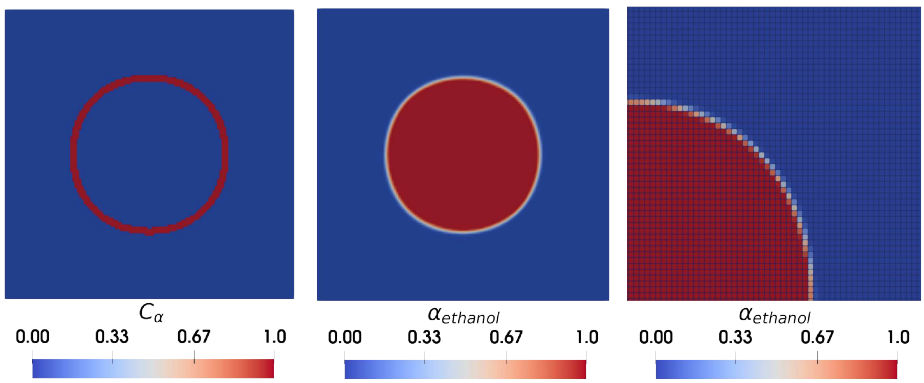

Figure 4: Contours of C_α switch (left), ethanol volume fraction (centre) and zoomed-in on the interfacial region (right).

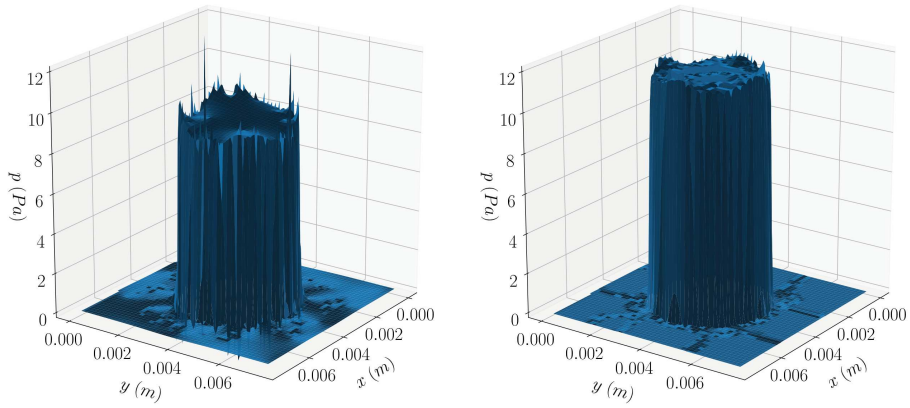

Figure 5: Calculated pressure field: VoF (left) and GEMMA (right).

view of the volume fraction field. This results in an interface thickness equal to approximately 2-3 times the mesh size, which is typical of interface-resolving approaches such as VoF.

In order to compare the performance of GEMMA with a standard interface-resolving approach, the same case has been simulated using *interFoam*, the standard VoF solver included in OpenFOAM, using the same mesh and numerical settings used with GEMMA. The pressure fields obtained with *interFoam* and GEMMA are depicted in Figure 5. Since GEMMA is based on a compressible solver, the value of the gauge pressure $p_g = p - p_{atm}$ is shown in the figure for this model. *interFoam* uses the standard CSF model without density correction for the calculation of the surface tension force, and this results in the presence of spurious pressure spikes at the interface; the use of a smoothed volume fraction field in the SCSF-based formulation implemented in GEMMA results in a significantly smoother pressure field. The resulting standard deviation of the pressure within the droplet is equal to 0.14 and 0.26 Pa for GEMMA and VoF, respectively.

The analytical pressure drop across the interface is equal 11.805 Pa [13]. The calculated pressure drop across the interface with *interFoam* and GEMMA, together with the reference analytical value, are reported in Table 6. It can be seen that the use of the SCSF approach together with an appropriate density correction results in a more accurate prediction of the pressure drop with the GEMMA approach, compared with standard CSF method used in *interFoam*. This also shows that the generalized multifluid surface tension implementation proposed in Equation (12) results in an accurate prediction of the pressure field in a case dominated by surface tension effects.

	Surface tension formulation	Δp (Pa)	Relative Error
Analytical	n/a	11.805	n/a
VoF (interFoam)	CSF	9.16	-22.41%
GEMMA	Multifluid SCSF	11.45	-3.01%

Table 6: Calculated pressure drop across the droplet interface.

	Density ρ (kg/m^3)	Viscosity μ $(Pa \cdot s)$
Air	1.1768	1.74e-5
Water	1000	0.001
σ (N/m)	0.07	

Table 7: Fluid properties for air and water.

4.2. Dam break in the presence of an obstacle

The collapse of a liquid column, also known as "dam break", is a typical test case for interface-resolving models [38, 39]. The experimental set-up used in [38], which includes the presence of an obstacle on the bottom wall, is considered here. The computational domain is a square of side equal to $4L$, where L is 0.146 m. At $t = 0$, a rectangular water column of width L and height $2L$ is initialized in the bottom-left corner of the domain. A rectangular obstacle of width ℓ and height 2ℓ (with ℓ equal to 0.024 m) is present at the centre of the bottom side of the square. The case has been investigated using three different structured quadrilateral grids with sizes equal to 48×48, 96×96 and 192×192 for the coarse, medium and fine mesh, respectively. All the boundaries are treated as no-slip walls, with the exception of the upper boundary which is a fixed pressure outlet. Both the water and the air phases are considered laminar and the physical properties used in the simulation are summarised in Table 7. The Schiller-Naumann drag model [24] is used for dispersed interfacial morphologies, with a constant dispersed phase diameter equal to 1 mm. The C_α switch is based on IRQ, with $IRQ_{crit} = 2$. All the simulations have been run for a flow time of 1 second.

The calculated water volume fraction contours 0.2 and 0.4 seconds after the collapse of the water column with the three different meshes are shown in Figure 6, together with the experimental snapshots taken from [38]. The figure also shows the local status of the C_α switch at the two flow times. Overall, it is observed that the numerical results obtained with GEMMA are in good qualitative agreement with the experiment, and also in this case the switching criterion is capable of identifying the position of the segregated/large-scale interface within the domain on all the considered meshes. This results in a sharp interface being maintained in the cells where $C_\alpha = 1$. The formulation for dispersed/small interfaces is used in the cells containing a mixture of the two phases for which $C_\alpha = 0$; as expected, the presence of such dispersed/small interface regions is reduced at increased mesh resolutions, as more and more interfacial scales are resolved using the large/segregated interfaces formulation.

A comparison between GEMMA (all three meshes) and the VoF results obtained with *interFoam* (medium mesh only) is shown in Figure 7, in terms of the predicted temporal evolution of the location of the interface at the left wall of the domain. All the simulation results are comparable up to $t \approx 0.8$ s, and all the numerical results are in a reasonable agreement with the experimental observations up to the experimental data point located $t \approx 0.5$ s. Successively, the increase in the height of the free surface is due to splashing phenomena on the left wall; the VoF method overestimates the location of the free surface at $t = 1$ s, whilst the GEMMA approach appears to underestimate it, although the agreement with the experimental data point improves with mesh refinement. The latter observation is probably due to the improved resolution of the entrainment of air bubbles under the free surface, as pointed out also in [38].

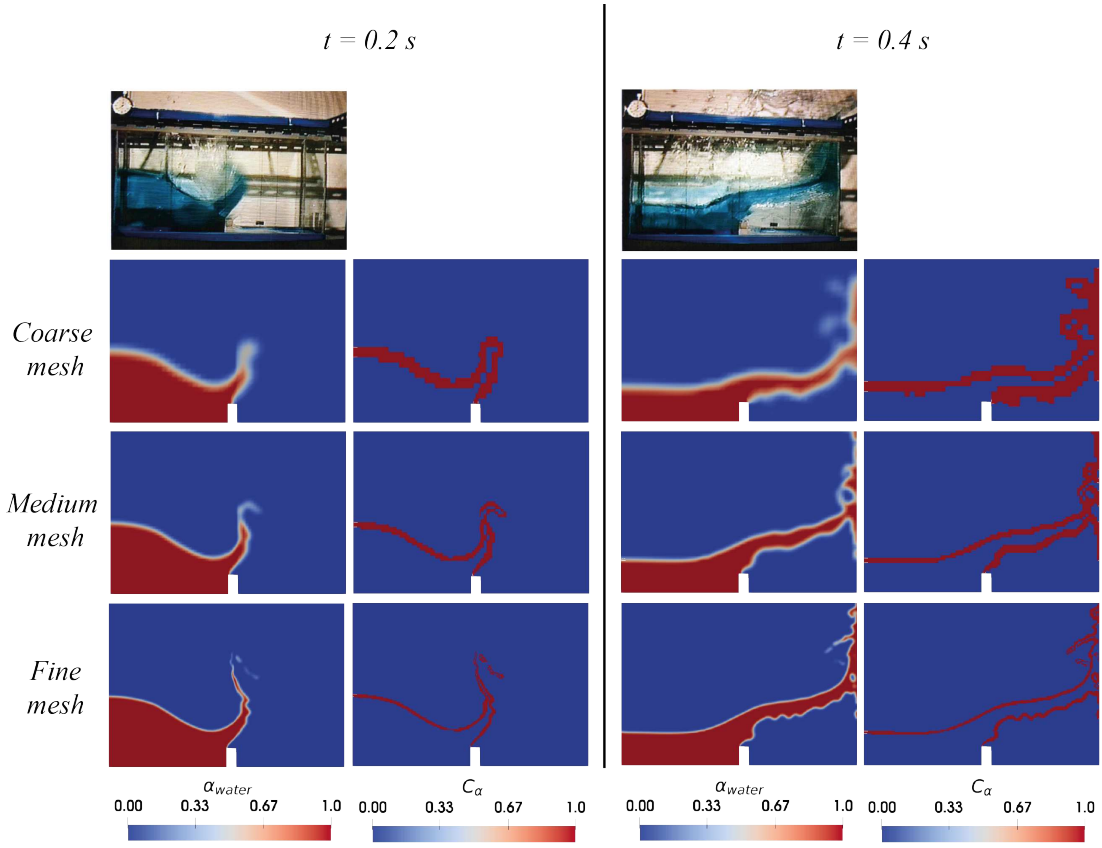

Figure 6: Calculated water volume fraction and C_α field at $t = 0.2$ (left) and 0.4 (right) seconds on the three numerical grids, compared with the corresponding experimental snapshots (reproduced from [38] with permission).

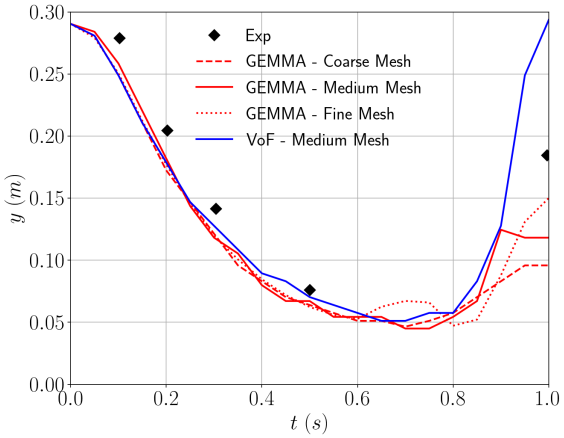

Figure 7: VoF (medium mesh) and GEMMA (all three meshes) predictions for the location of the interface on the left wall of the domain over time, compared against the experimental data reported in [38].

	Density ρ (kg/m^3)	Viscosity μ $(Pa \cdot s)$
Gas	100	1
Liquid	1000	10
σ (N/m)	24.5	

Table 8: Fluid properties for the raising bubble test case.

4.3. Rising bubble

Another typical test case used to assess the accuracy of multiphase models is a bubble rising in a stagnant liquid. The case is relatively simple and has the advantage of having a benchmark solution available from the work of [40] in which the authors compared the results of three different interface capturing codes based on the Level Set method and reported consistent and very similar solutions for the bubble rising velocity, rising height and shape. This benchmark was recently used by [27] to evaluate the performance of their own hybrid solver HD-LIS. Here, the first test from the benchmark of [40] is simulated with the GEMMA approach.

A bubble of diameter 0.5 m is suspended in a two-dimensional liquid domain of height 2 m and width 1 m. The initial position of the bubble is on the vertical bisector, 0.5 m above the bottom of the domain. The fluid properties are reported in Table 8. These values result in an Eötvös ($Eo = \frac{\Delta \rho g d^2}{\sigma}$) and a Morton ($Mo = \frac{\Delta \rho g \mu_c^4}{\rho_c^4 \sigma^3}$) number equal to 9.0 and 6 x 10^{-4}, respectively. From the Grace diagram [46], where the shape of a bubble rising in stagnant liquid is identified based on these two non-dimensional numbers, the given properties correspond to a bubble of ellipsoidal shape. For this case, only drag and surface tension were considered in the interfacial momentum transfer. Drag for large scale interfaces is evaluated from [2], and for dispersed interfaces from the correlation of Tomiyama et al. [42]. The domain is discretised with a 80×160 uniform mesh. Free slip and no slip boundary conditions are applied to the lateral and horizontal walls, respectively. The gravitational acceleration is fixed to 0.98 ms^{-2}, following [40], and the flow is considered laminar for both fluids. The simulation was run for 3 s, with a time-step size adjusted to maintain the Courant number below 0.25.

Figure 8 shows the evolution of the bubble volume fraction, the C_α field and the pressure field at three different time instants. The bubble, starting from a spherical shape, rises in the surrounding water and deforms, reaching and maintaining the expected ellipsoidal shape towards the end of the simulation. For the entire simulation time, the interface is kept sharp by the compression algorithm. As clearly shown in Figure 8, the switching logic successfully activates C_{alpha} at the bubble/liquid interface only. Inside the bubble, the pressure is higher with respect to the surrounding liquid, as expected.

Quantitative comparisons with the reference data of [40] are provided in Figure 9, where the mean rising velocity of the bubble and its average height in the domain are provided as a function of time. Their values are evaluated from an average of the cell values weighted by the bubble volume fraction. The results obtained with the VoF solver *interFoam* are also shown in the figure. The accuracy of the GEMMA approach is satisfactory, with the predictions being in substantial agreement with interface capturing methods, except for the tendency of GEMMA to slightly underpredict the rising velocity in the first second of the transient; this is probably due to an overprediction of the drag with the model given in Equation (18). Later on, remarkable accuracy is obtained and GEMMA even outperforms *interFoam*. The lower rising velocity at the beginning of the transient results in a slight delay in the rising height predicted by GEMMA that is maintained, but does not increase, until the end of the transient.

4.4. Dispersed flow in a vertical pipe

The previous test cases were focused on assessing GEMMA against interface capturing methods in cases that required maintenance of a sharp interface. In this case the GEMMA approach is employed to predict a dispersed bubbly flow in a vertical pipe, with the aim of testing the dispersed

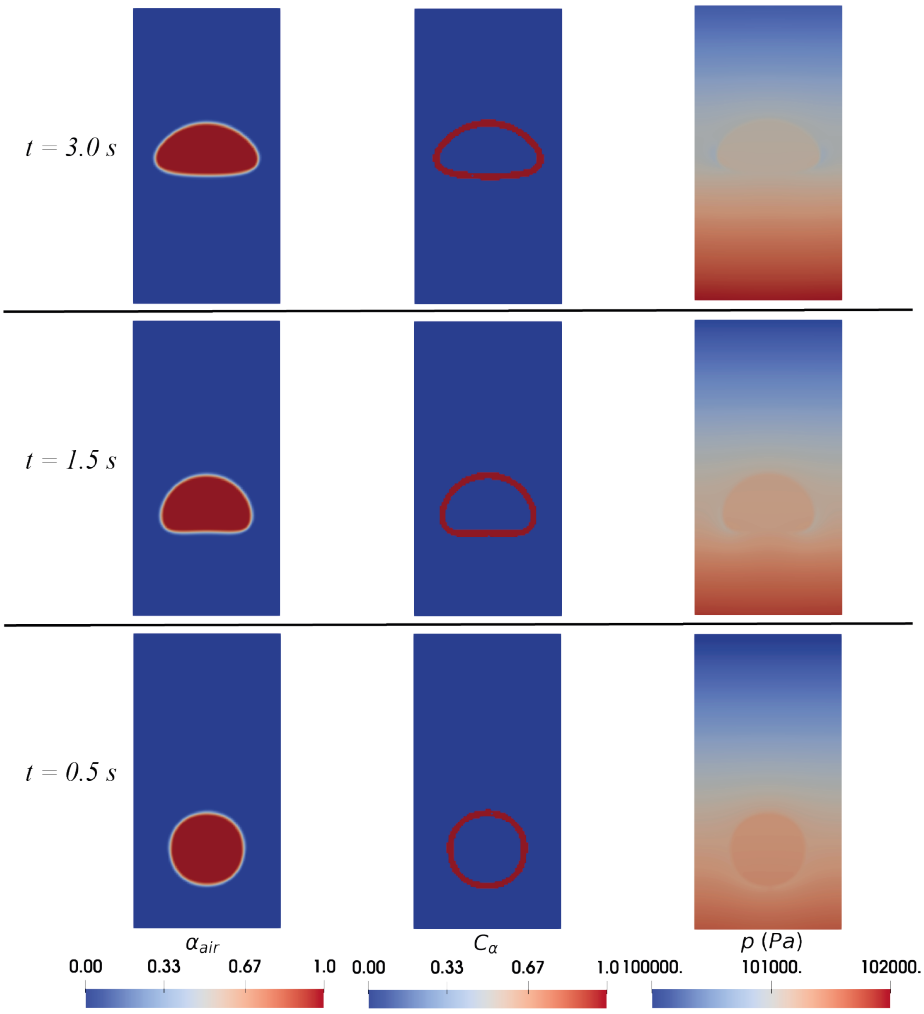

Figure 8: GEMMA prediction of the rising bubble test case from Hysing et al. [40]. From left to right, the bubble volume fraction, the switch coefficient C_α and the pressure are shown at three different times.

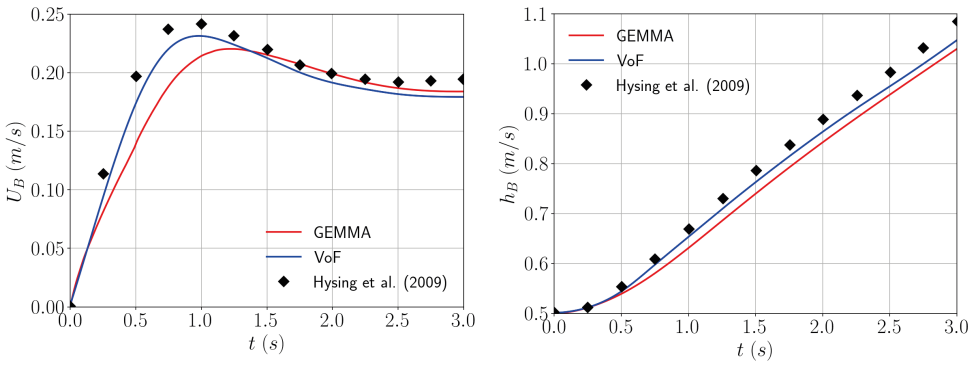

Figure 9: GEMMA predictions of mean bubble rising velocity (left) and rising height (right) compared against Hysing et al. [40] and the *interFoam* VoF solver.

multifluid framework. The test case is taken from the air-water bubbly flow experiment of Hosokawa and Tomiyama [43] in a pipe with an inner diameter 25 mm. The case has a water superficial velocity $j_l = 1.0\ ms^{-1}$ and air superficial velocity $j_g = 0.036\ ms^{-1}$. The average void fraction is $\alpha = 0.033$ and the average bubble diameter d_B, which is kept constant in the entire domain, is 3.66 mm. These operating conditions correspond to a low void, dispersed bubbly flow; therefore, interface compression should not activate and C_α should be equal to zero everywhere. In order to predict the void distribution correctly, all the contributions to interfacial momentum transfer (Equation (13)) are included in the model. The dispersed drag is modelled with [42] and the lift with the correlation of Tomiyama et al. [47]. Wall force and turbulent dispersion are evaluated with the models of Antal et al. [48] and Burns et al. [49], respectively. Turbulence is considered in the liquid phase with a multiphase extension of the standard $k-\varepsilon$ model, whilst laminar flow is assumed for the air phase. A quarter section of the pipe is modelled, with symmetry boundary conditions on the two lateral sides and a no-slip condition at the wall. The velocity of the phases and the void fraction value are fixed at the inlet section, whilst the pressure value is imposed at the outlet section; a zero gradient condition is employed for all the other variables. Based on previous experience in the modelling of the same experiment [41], the domain is discretised using 64×480 structured cells (cross sectional area $\times$ length). The physical properties of the two phases are summarised in Table 7.

The evolution of the air void distribution along the pipe is visualised in Figure 10. The void fraction is homogeneous at the inlet section but, under the action of the lift force, which is positive for bubbles having a nearly spherical shape such as those observed in this experiment, the bubbles tend to accumulate towards the wall. The presence of the wall then confines the bubbles, and a typical wall-peaked radial void fraction profile is observed, as shown in the plot of the radial experimental void fraction profile shown in Figure 10. The shifting of the void fraction towards the wall is clear in the numerical results reported in Figure 10, which confirms that the model correctly operates in the multifluid dispersed-interface mode. The quantitative comparison in Figure 10 shows that the GEMMA approach can reproduce the main features of the void fraction distribution, although the void fraction accumulation at the wall is over predicted, probably as a consequence of a too weak wall force. However, the focus of the present work is to assess the applicability of the approach across multiple flow regimes. Therefore, further improvement of the multifluid closure framework was not pursued at this stage and will be addressed in future research.

4.5. Water jet plunging in a quiescent pool

A water jet plunging in a quiescent pool is a prototypical example of a multiphase flow encompassing a broad range of interfacial scales, from the segregated interface found at the free surface of the pool to the bubbles of different sizes formed by the entrained air [50]. Therefore, it is an ideal case to assess the multiscale capabilities of multiphase modelling approaches [18, 44].

For the present test with GEMMA we consider the same case and numerical set-up used in [44], which is based on the experimental set-up of [45]. The physical properties of the two phases are reported in Table 7. The computational domain is depicted in Figure 11. The domain has a square section of side 0.1 m and a height of 0.3 m; the domain is filled with water up to 0.2 m from the bottom, leading to a jet length L_j of 0.1 m. The plunging water jet enters the domain through a circular pipe of diameter equal to 0.006 m with an average velocity v_0 equal to 1.5 m/s and a fully developed velocity profile. These parameters correspond to a Reynolds number within the pipe equal to 9000 and a jet velocity at impact on the free surface $v_j = \sqrt{v_0^2 + 2gL_j}$ equal to 2.05 m/s.

A constant water mass flow rate equal to that entering through the inlet pipe is enforced at the outlet, in order to keep the free surface level constant. The no-slip condition is enforced on all the walls, whilst the top surface is considered open to the atmosphere, where a *totalPressure* boundary condition is used for the pressure. A 0.02×0.02 m square outlet section is located at the bottom of one side of the domain, as shown in Figure 11; a *fixedFluxPressure* condition is used on this boundary for the pressure. The reference medium mesh is the same as that used by [44], and consists of about 3.03M hexahedra of 1 mm size; for the sake of assessing the sensitivity of the model to mesh resolution, two additional simulations have been performed on meshes with size

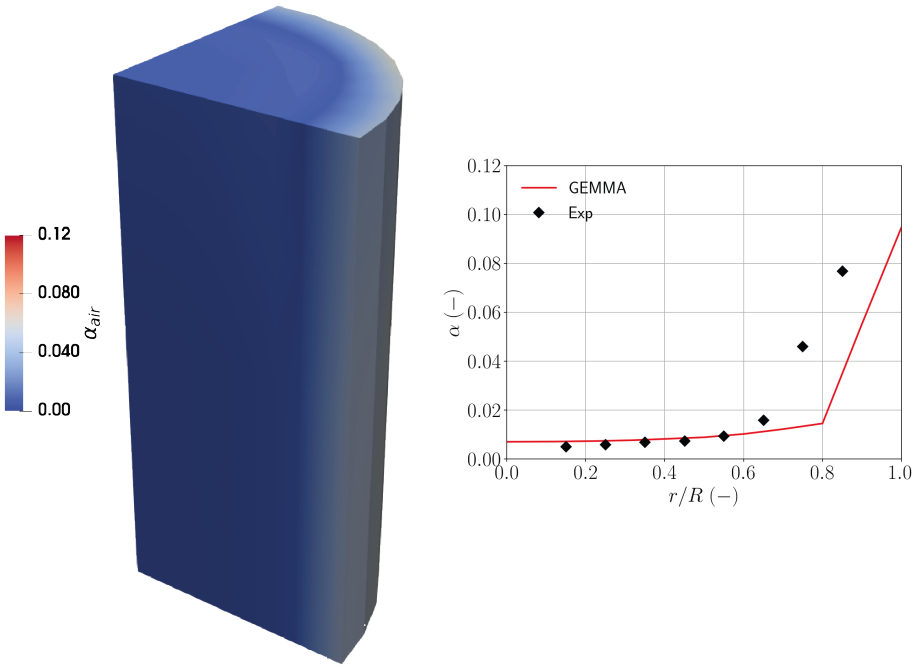

Figure 10: Evolution of the void distribution in the pipe (left) and comparison of GEMMA predictions of the radial void profile against experimental data from Hosokawa and Tomiyama [43].

equal to 2 mm and 0.5 mm, resulting in a cell count of about 378k and 24.0M for the coarse and the fine mesh, respectively. The air phase is considered to be laminar, whilst a LES approach with the standard Smagorinsky closure for the subgrid-scale stresses is used for the water phase [51]. A flow-time of 2 s has been simulated.

The One Primary-One Secondary Particle Model (OPOSPM) [52] is used as a reduced population balance to estimate the diameter of the dispersed air phase; this is a one-group population balance which solves a single transport equation for the total number density N_d. The kernels of Martinez-Bazan [53] and Prince-Blanch [54] are used to evaluate break-up and coalescence rates, respectively, within the number density equation. Such a simplified approach is used to keep computational costs to a minimum, since the main goal here is to demonstrate the multiscale capabilities of the numerical model. Nevertheless, it should be pointed out that the GEMMA method is fully compatible with more complex multi-group population balance approaches. Since the local diameter of the dispersed phase is known from the population balance, the switch method used within GEMMA is based on both IRQ and the dispersed phase diameter, as detailed in Section 2.1, with $IRQ_{crit} = 2$ and $\Gamma = 2$ for all the three meshes. Also, the Schiller-Naumann model [24] is used to evaluate the dispersed-interface drag force, with a variable dispersed phase diameter equal to the mean diameter evaluated via the population balance.

A qualitative comparison between the numerical results obtained on both meshes and experimental snapshots reported in [18] for the initial transient up to $t = 0.015$ seconds is reported in Figure 12; it should be pointed out that only a qualitative comparison with the experimental snapshots is reported here, and that the snapshots refer to an experimental case with a jet impact velocity v_j equal to 2.3 m/s (information on the corresponding values of v_0 and L_j in the experiment were not reported in the experimental work [55]). With respect to the reference mesh, at $t = 0.009$ seconds the jet just impinged the free surface and there is no significant presence of entrained air bubbles; instead, a distinctive air cavity is observed in the experiments, which is well captured by the numerical simulation. It is also worth noting that the large-scale mode is activated in GEMMA for the plunging jet/air interface above the free surface as well as for the water/air interface at the

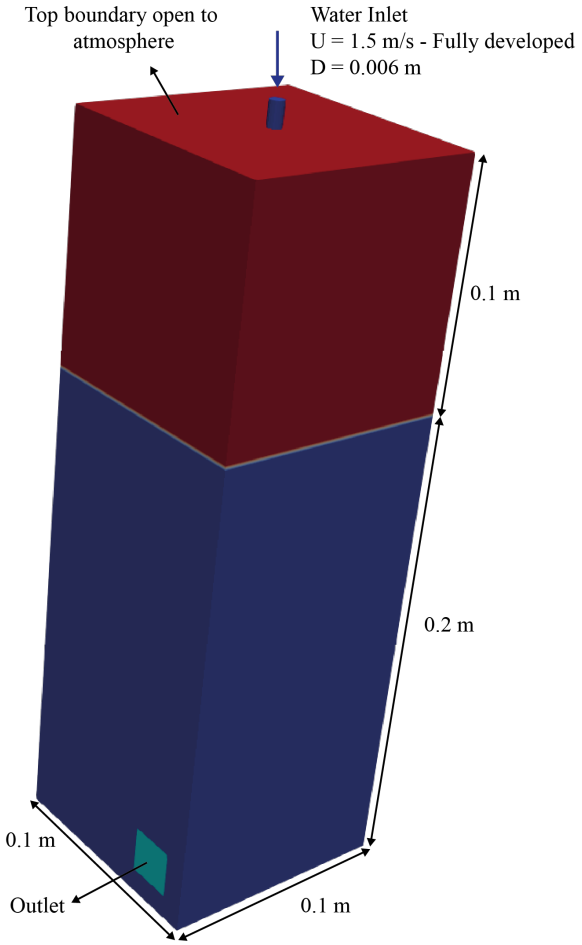

Figure 11: Computational domain for the plunging jet case.

free surface; in addition, interface compression is enforced for the interface between the air cavity and the surrounding water. At $t = 0.012$ seconds pinch-off of the air cavity has happened and air bubbles start to be entrained and this is again well predicted by the simulation; interface resolution is active for the large bubble resulting from the pinch-off, whilst the smaller entrained bubbles close to the free surface are accounted for in interface-averaging mode. At subsequent instants, the large bubble deforms ($t = 0.014$ s) and breaks down ($t = 0.015$ s) into two smaller structures, which eventually begin to raise towards the free surface due to buoyancy; at the same time, more and more air is entrained in the form of a myriad of relatively small bubbles. The GEMMA approach is capable to qualitatively reproducing all these phenomena; the two larger bubbles clearly visible in the experiments at $t = 0.015$ seconds are still treated in large-interface mode, whilst the entrainment of the smaller bubbles is treated using the interface-averaging mode.

With respect to the sensitivity of the modelling approach to mesh resolution, the results obtained with the different meshes are generally consistent with each other in terms of the main flow features, i.e. formation of an air cavity right after the impingement, pinch-off of the cavity tip, entrainment of air bubbles and upward motion of these bubbles due to buoyancy. For the initial transient shown in Figure 12, the large/segregated interface mode is activated with all the meshes for the interfacial regions associated with the free jet and the free surface of the pool, although it is interesting to note that the smaller interfacial scales observed at the free surface in the area of the jet impact imply that this region is not treated with the large/segregated interface formulation on the coarse mesh. More striking differences are observed with respect to the treatment of the entrained air within the pool: the size of the coarse mesh is not small enough to guarantee an adequate resolution of the air cavity and of the large bubble observed immediately after pinch-off; as a consequence, these features are treated in the small/dispersed interface mode on the coarse mesh. Likewise, the two large bubbles present in the experiments at $t = 0.015$ seconds and the dispersed-to-segregated transition observed on the finer meshes due to the coalescence of the air bubbles within the pool (discussed more in detail below) are not observed on the coarse mesh, and this is due to the fact that the latter does not guarantee an adequate resolution of the interfacial scales associated with these relatively large bubbles. Overall, it appears that the penetration depth of the entrained air (e.g.: depth of the cavity, location of the large bubbles) tends to increase as the numerical grid is refined. As mentioned also below when discussing the results obtained for the penetration depth of the bubble plume, this is probably due to an overestimation of the drag force evaluated with the considered "dispersed" drag closure [24] and to the fact that the impact of this closure on the results becomes less significant as the mesh gets refined and more air bubbles are treated using the segregated/large interface formulation. It is concluded that, as expected, a coarsening of the mesh results in the "standard" dispersed multifluid formulation being applied to more and more interfacial scales for a given test case, as the capability of the mesh to provide an adequate (as specified by the user via the model coefficients IRQ_{crit} and Γ) resolution of the interfacial scales reduces as a result of the coarsening; as a consequence, the closures used for the modelling of the interfacial transfer terms due to the presence of "subgrid" DPEs become more and more important as the mesh is coarsened.

After an initial transient the flow essentially consists of a downward motion caused by the plunging jet coupled with the buoyancy-driven upward motion of the bubbles surrounding the jet [45]. The penetration depth H_p is the lowest point reached by the bubble plume at a given instant; due to the turbulent nature of the flow, this can fluctuate depending on the considered instantaneous realisation [56]. Experimentally, a representative time-averaged H_p value is usually evaluated using image analysis techniques [55, 56] and an equivalent procedure has been used to extrapolate the time-averaged bubble penetration depth from the present CFD simulations. Figure 13 shows the penetration depth obtained with GEMMA on the three different meshes compared with the experimental value reported in [55] for $v_0 = 1.6$ m/s and $L_j = 0.1$ m. It can be observed that a better agreement with the experimental measurement is observed on the finer meshes, and this is probably due to a more accurate resolution of the drag force when most of the entrained air bubbles are treated using the large/segregated interface formulation (as it is the case with finer meshes) as

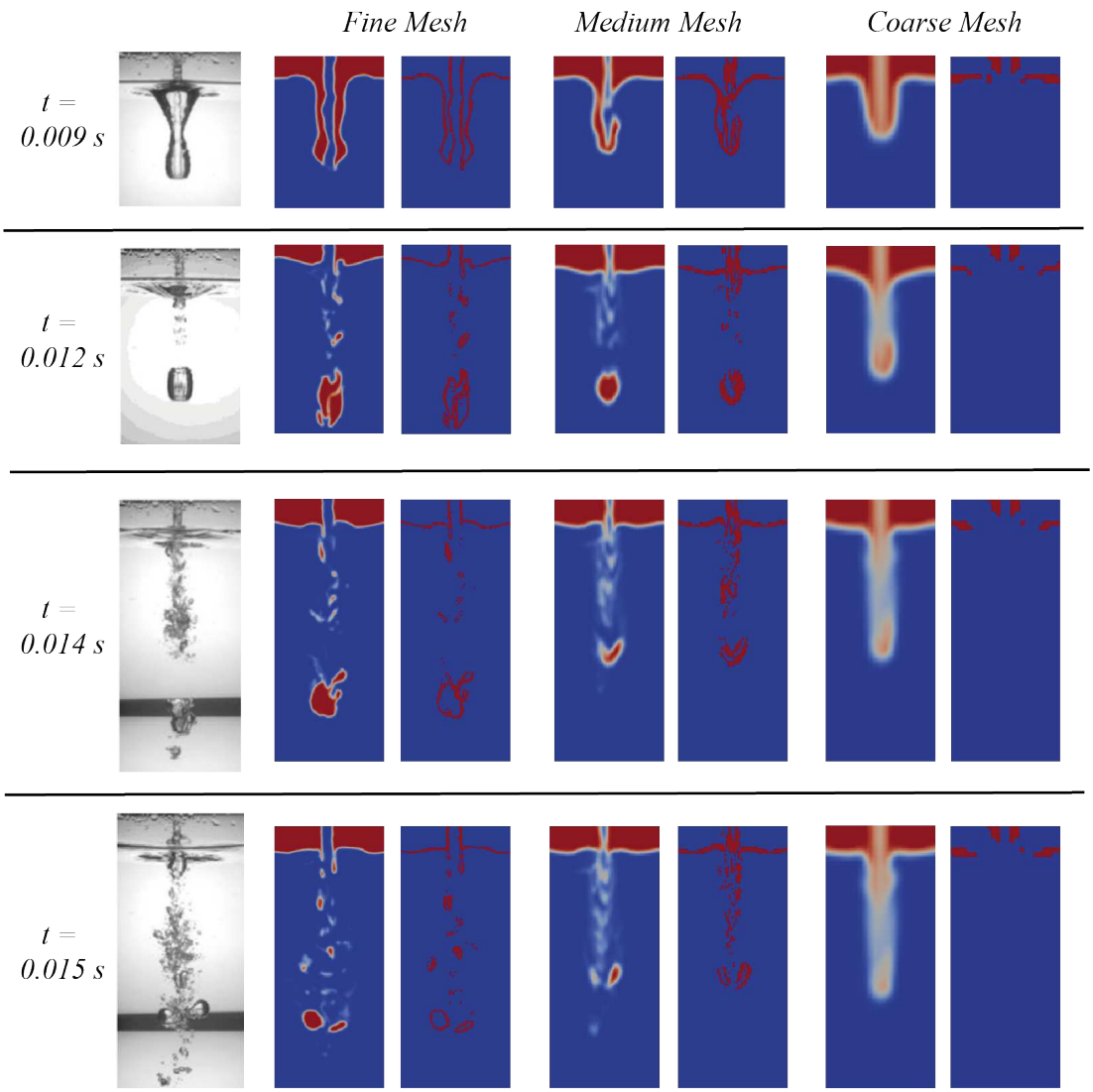

Figure 12: From left to right: experimental snapshots (reproduced from [18] with permission) and numerical results obtained on the different meshes for the air volume fraction and C_α field on the mid-plane at four different flow times.

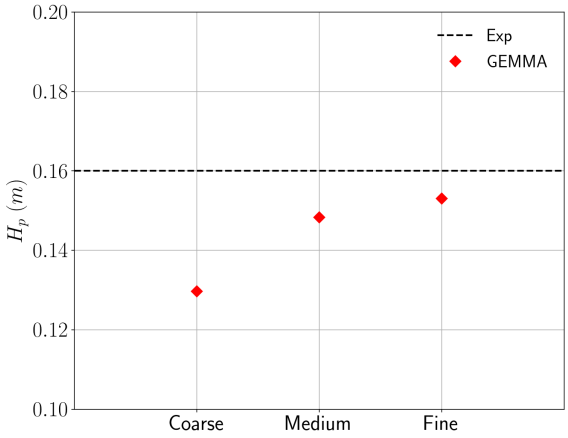

Figure 13: Calculated penetration depth on the three meshes against the experimental value of reported in [55].

opposed to being treated as "sub-grid" dispersed DPEs (as it is the case on coarser meshes); in the latter case, the specific closures used for the "sub-grid" interfacial momentum transfer play a significant role in the evaluation of the penetration depth.

Occasionally the entrained bubbles will coalesce and form larger cap-shaped air bubbles; the coalescence of small subgrid-scale bubbles into larger structures that can be treated in large-interface mode is a particularly challenging phenomenon to capture numerically [18]. This mechanism is shown qualitatively in Figure 14, which reports the formation of a large cap-shaped bubble via coalescence of dispersed subgrid-scale bubbles from $t = 1.35$ to $t = 1.44$ seconds on the medium mesh. At $t = 1.35$ s the small dispersed bubbles start to coalesce and result in the formation of a pear-shaped large bubble at $t = 1.35$ s; this results in the activation of the large-interface mode for this bubble. Subsequently, this bubble starts to raise under the effect of buoyancy ($t = 1.44$ s) and acquires its characteristic cap shape ($t = 1.44$ s). The large-interface, active when $C_\alpha = 1$, allows for the correct prediction of the shape of the bubble, which is retained during its upward motion towards the free surface, and avoids the smearing effects which would be observed with a standard multifluid model; the interface compression term in Equation (3) plays a key role in avoiding interface smearing, similarly to the "clustering" term included in the GENTOP model [38]. Although the capability of GEMMA to reconstruct the morphology of the interface during the dispersed-to-segregated transition demonstrated qualitatively above is an encouraging achievement, a more quantitative and precise assessment of the proposed approach in this respect will be needed in the future; in this regard, it is highlighted that the treatment of the dispersed-to-segregated transition in the context of multiscale approaches is still an open field of research and further model development and assessment in this respect will be performed in future work, considering other multiscale flow configurations available in the literature [57, 58].

5. Conclusions

A novel GEneralized Multifluid Modelling Approach (GEMMA) for the simulation of multiscale multiphase flows of practical interest has been developed and assessed, in order to overcome the limitations of the standard interface-averaging and interface-resolving approaches. The proposed approach uses a binary function to switch between large-interface and dispersed-interface mode locally. The switch status also controls relevant terms in the governing equations such as the surface tension force and the blending between interfacial transfer models suitable for small/dispersed and large/segregated interfaces. The switch logic is based on the local resolution of the interfacial scales and allows control of the minimum level of interface resolution needed to activate the

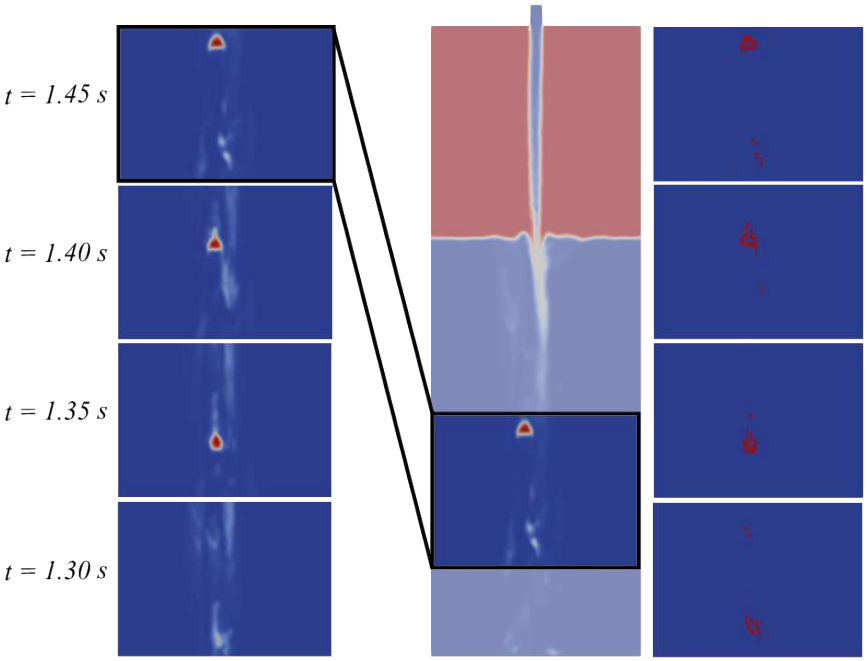

Figure 14: Resolution of a large cap-shaped bubble formed via coalescence of smaller sub-grid size bubbles on the medium mesh: transient evolution of the volume fraction (left) and C_α (right) fields.

large-interface mode. The modelling approach has been assessed in different test cases and demonstrated to have an accuracy comparable to standard interface-resolving approaches such as VoF in typical large/segregated-interface flow cases, whilst a standard multifluid behaviour is recovered for dispersed flows; this makes it an attractive solution for the simulation of flows characterised by the coexistence of different interfacial morphologies. Furthermore, the simulation of a prototypical multiscale flow showed that the approach can effectively switch between large-interface and dispersed-interface mode based on the local flow conditions and mesh resolution. The proposed modelling concept can also predict the formation of large "resolved" structures via coalescence of smaller subgrid-scale dispersed elements. It is concluded that GEMMA represents a promising step towards the development of a comprehensive multiscale modelling approach for multiphase flows of practical relevance. Future work will focus on the full integration of the switch logic within GEMMA with the population balance equations, the refinement of interfacial transfer sub-models and further assessment in complex cases of industrial relevance.

Declaration of competing interest

None declared.

Acknowledgements

This work was supported by the EU project GENIORS (Project ID: 755171) on GEN IV Integrated Oxide Fuels Recycling Strategies and the EPSRC through grant EP/S019871/1, Towards Comprehensive Multiphase Flow Modelling for Nuclear Reactor Thermal Hydraulics . The authors are also grateful to Kent Wardle for sharing the source code of his solver and for his inputs to the present research work.

References

[1] A. Prosperetti, G. Tryggvason, Computational Methods for Multiphase Flow, Cambridge University Press, Cambridge, 2007.

[2] H. Marschall, Towards the numerical simulation of multi-scale two-phase flows, Ph.D. thesis, Technische Universität München (2011).

[3] M. Sussman, E. G. Puckett, A coupled level set and volume-of-fluid method for computing 3D and axisymmetric incompressible two-phase flows, Journal of Computational Physics 162 (2000) 301–337.

[4] C. Hirt, B. Nichols, Volume of fluid VOF method for the dynamics of free boundaries, Journal of Computational Physics 39 (1) (1981) 201 – 225.

[5] O. Ubbink, Numerical prediction of two fluid systems with sharp interfaces, Ph.D. thesis, Imperial College (1997).

[6] K. G. Lyras, B. Hanson, M. Fairweather, P. J. Heggs, A coupled level set and volume of fluid method with a re-initialisation step suitable for unstructured meshes, Journal of Computational Physics (2020) 109224.

[7] D. W. Theobald, B. Hanson, M. Fairweather, P. J. Heggs, Implications of hydrodynamics on the design of pulsed sieve-plate extraction columns: A one-fluid multiphase CFD model using the volume of fluid method, Chemical Engineering Science 221 (2020) 115640.

[8] D. Bestion, Applicability of two-phase CFD to nuclear reactor thermalhydraulics and elaboration of best practice guidelines, Nuclear Engineering and Design 253 (2012) 311–321.

[9] G. Cerne, S. Petelin, I. Tiselj, Coupling of the interface tracking and the two-fluid models for the simulation of incompressible two-phase flow, Journal of Computational Physics 171 (2001) 776–804.

[10] K. Yan, D. Che, A coupled model for simulation of the gas–liquid two-phase flow with complex flow patterns, International Journal of Multiphase Flow 36 (4) (2010) 333–348.

[11] A. Tomiyama, K. Sakoda, K. Hayashi, A. Sou, N. Shimada, S. Hosokawa, Modeling and hybrid simulation of bubbly flow, Multiphase Science and Technology 18 (2006) 73 – 110.

[12] A. Alajbegovic, J. Han, Simulation of multiphase flows in complex geometry using a hybrid method combining the multi-fluid and the volume-of-fluid (VOF) approaches, in: ASME Joint U.S.-European Fluids Engineering Conference (Fluids2002), 2002.

[13] L. Štrubelj, I. Tiselj, B. Mavko, Simulations of free surface flows with implementation of surface tension and interface sharpening in the two-fluid model, International Journal of Heat and Fluid Flow 30 (4) (2009) 741–750.

[14] V. H. Gada, M. P. Tandon, J. Elias, R. Vikulov, S. Lo, A large scale interface multi-fluid model for simulating multiphase flows, Applied Mathematical Modelling 44 (2017) 189–204.

[15] E. Olsson, G. Kreiss, A conservative level set method for two phase flow, Journal of Computational Physics 210 (2005) 225 – 246.

[16] L. Strubelj, I. Tiselj, Two-fluid model with interface sharpening, International Journal of Numerical Methods in Engineering 85 (2011) 575 – 590.

[17] H. Marschall, O. Hinrichsen, Numerical simulation of multi-scale two-phase flows using a hybrid interface-resolving two-fluid model (hires-tfm), Journal of Chemical Engineering of Japan 46 (2013) 517 – 523.

[18] S. Hänsch, D. Lucas, E. Krepper, T. Höhne, A multi-field two-fluid concept for transitions between different scales of interfacial structures, International Journal of Multiphase Flow 47 (2012) 171–182.

[19] T. Höhne, C. Vallée, Experiments and numerical simulations of horizontal two-phase flow regimes using an interfacial area density model, The Journal of Computational Multiphase Flows 2 (3) (2010) 131–143.

[20] E. Krepper, D. Lucas, T. Frank, H.-M. Prasser, P. J. Zwart, The inhomogeneous MUSIG model for the simulation of polydispersed flows, Nuclear Engineering and Design 238 (7) (2008) 1690–1702.

[21] P. Coste, A large interface model for two-phase CFD, Nuclear Engineering and Design 255 (2013) 38–50.

[22] K. E. Wardle, Hybrid multiphase CFD simulation for liquid-liquid interfacial area prediction in annular centrifugal contactors, in: Proceeding of the Global 2013, Salt Lake City, Usa, 2013.

[23] K. E. Wardle, H. G. Weller, Hybrid multiphase CFD solver for coupled dispersed/segregated flows in liquid-liquid extraction, International Journal of Chemical Engineering 2013 (2013) 1–13.

[24] L. Schiller, A. Naumann, A drag coefficient correlation, Zeitschrift des Vereins Deutscher Ingenieure 77 (1935) 318 – 320.

[25] J. U. Brackbill, D. B. Kothe, C. Zemach, A continuum method for modeling surface tension, Journal of computational physics 100 (2) (1992) 335–354.

[26] D. Papoulias, V. Gada, M. Tandon, S. Lo, CFD modelling of multiphase slug flow in a pressurized water reactor using the Eulerian - Eulerian model and Adaptive Interface Sharpening Scheme, in: 17th International Topical Meeting on Nuclear Reactor Thermal Hydraulics (NURETH-17), 2017.

[27] A. Mathur, D. Dovizio, E. Frederix, E. Komen, A hybrid dispersed-large interface solver for multi-scale two-phase flow modelling, Nuclear Engineering and Design 344 (2019) 69–82.

[28] J. A. Heyns, O. F. Oxtoby, Modelling surface tension dominated multiphase flows using the VOF approach, in: 6th European Conference on Computational Fluid Dynamics, 2014, pp. 7082–7090.

[29] H. G. Weller, G. Tabor, H. Jasak, C. Fureby, A tensorial approach to computational continuum mechanics using object-oriented techniques, Computers in Physics 12 (6) (1998) 620–631.

[30] The OpenFOAM Foundation, OpenFOAM - User Guide, 6th Edition (2018).

[31] E. Berberovic, N. P. van Hinsberg, S. Jakirlic, I. V. Roisman, C. Tropea, Drop impact onto a liquid layer of finite thickness: Dynamics of the cavity evolution, Physical Review E 79 (2009) 036306.

[32] J. Anez, F. Demoulin, N. Hecht, J. Reveillon, A general purpose LES model for atomization, in: European Conference Liquid Atomization & Spray Systems, 2016.

[33] J. Nahed, J. Dgheim, Estimation curvature in PLIC-VOF method for interface advection, Heat and Mass Transfer (2019) 1–15.

[34] T. Höhne, J. P. Mehlhoop, Validation of closure models for interfacial drag and turbulence in numerical simulations of horizontal stratified gas–liquid flows, International Journal of Multiphase Flow 62 (2014) 1 – 16.

[35] K. J. Vachaparambil, K. E. Einarsrud, Comparison of surface tension models for the volume of fluid method, Processes 7 (8) (2019) 542.

[36] S. Patankar, D. Spalding, A calculation procedure for heat, mass and momentum transfer in three-dimensional parabolic flows, International Journal of Heat and Mass Transfer 15 (10) (1972) 1787 – 1806.

[37] R. Issa, Solution of the implicitly discretised fluid flow equations by operator-splitting, Journal of Computational Physics 62 (1) (1986) 40 – 65.

[38] S. Hänsch, D. Lucas, T. Höhne, E. Krepper, Application of a new concept for multi-scale interfacial structures to the dam-break case with an obstacle, Nuclear Engineering and Design 279 (2014) 171 – 181.

[39] C. Yu, H. Wen, Z. Gu, R. An, Numerical simulation of dam-break flow impacting a stationary obstacle by a CLSVOF/IB method, Communications in Nonlinear Science and Numerical Simulation 79 (2019) 104934.

[40] S. Hysing, S. Turek, D. Kuzmin, N. Parolini, E. Burman, Ganesan, L. Tobiska, Quantitative benchmark computations of two dimensional bubble dynamics, International Journal of Numerical Methods in Fluids 60 (2009) 1259 – 1288.

[41] M. Colombo, M. Fairweather, Multiphase turbulence in bubbly flows: RANS simulations, International Journal of Multiphase Flow 77 (2015) 222 – 243.

[42] A. Tomiyama, G. Celata, Hosokawa, S., S. Yoshida, Terminal velocities of single bubbles in surface tension force dominant regime, International Journal of Multiphase Flow 28 (2002) 1497 – 1519.

[43] S. Hosokawa, A. Tomiyama, Multi-fluid simulation of turbulent bubbly pipe flow, Chemical Engineering Science 64 (2009) 5308 – 5318.

[44] O. Y. Shonibare, K. E. Wardle, Numerical investigation of vertical plunging jet using a hybrid multifluid–VOF multiphase CFD solver, International Journal of Chemical Engineering 2015 (2015) 1–14.

[45] X. Qu, L. Khezzar, D. Danciu, M. Labois, D. Lakehal, Characterization of plunging liquid jets: A combined experimental and numerical investigation, International Journal of Multiphase Flow 37 (7) (2011) 722 – 731.

[46] J. Grace, T. Wairegi, T. Nguyen, Shapes and velocities of single drops and bubbles moving freely through immiscible liquids, Chemical Engineering Research and Design 54 (1976) 167 – 173.

[47] A. Tomiyama, H. Tamai, I. Zun, S. Hosokawa, Transverse migration of single bubbles in simple shear flows, Chemical Engineering Science 57 (2002) 1849 – 1858.

[48] S. Antal, R. Lahey, J. Flaherty, Analysis of phase distribution in fully developed laminar bubbly two-phase flow, International Journal of Multiphase Flow 17 (1991) 635 – 652.

[49] A. Burns, T. Frank, I. Hamill, J. M. Shi, The favre averaged drag model for turbulent dispersion in eulerian multi-phase flows, in: 5th International Conference on Multiphase Flows, 2004.

[50] Y. Zhu, H. N. Oguz, A. Prosperetti, On the mechanism of air entrainment by liquid jets at a free surface, Journal of Fluid Mechanics 404 (2000) 151–177.

[51] J. Smagorinsky, General circulation experiments with the primitive equations, Monthly Weather Review 91 (3) (1963) 99–164.

[52] C. Drumm, M. Attarakih, M. W. Hlawitschka, H. Bart, One-group reduced population balance model for CFD simulation of a pilot-plant extraction column, Industrial and Engineering Chemistry Research 49 (7) (2010) 3442–3451.

[53] C. Martinez-Bazan, J. L. Montanes, J. C. Lasheras, On the breakup of an air bubble injected into a fully developed turbulent flow, Journal of Fluid Mechanics 401 (1999) 157–182.

[54] M. J. Prince, H. W. Blanch, Bubble coalescence and break-up in air-sparged bubble columns, AIChE Journal 36 (10) (1990) 1485–1499.

[55] D. V. Melzer, Experimental investigation of impinging liquid jets with gas entrainment, Ph.D. thesis, Technische Universität Dresden (2018).

[56] M. Schmidtke, D. Danciu, L. Dirk, Air entrainment by impinging jets: Experimental identification of the key phenomena and approaches for their simulation in CFD, in: 17th International Conference on Nuclear Engineering - ICONE17, 2009, pp. 297–305.

[57] S. Vincent, L. Osmar, J. L. Estivalezes, S. Zaleski, F. Auguste, W. Aniszewski, Y. Ling, T. Menard, A. Pedrono, J. Magnaudet, J. P. Caltagirone, A. Berlemont, S. Popinet, A phase inversion benchmark for multiscale multiphase flows (2019). `arXiv:1906.02655`.

[58] J. Fabre, L. Masbernat, C. Suzanne, Experimental data set no. 7: stratified flow, part I: local structure, Multiphase Science and Technology 3 (1-4) (1987) 285–301.